ORIGINAL CONTRIBUTION

Study on the formation mechanism of hydrothermal prefabricated activated carbon and its adsorption capacity for malachite green

Xin Cui[1] · Didi Gai[1] · Baian Zhu[1] · Tong Wu[1] · Jing Zhang[1] · Peitao Zhao[1]

Abstract

The activated carbon (AC) adsorbents were prepared by KOH activation of hydrothermally pretreated pine sawdust (PS). The physicochemical properties of AC were characterized by scanning electron microscopy (SEM), Fourier transform infrared spectrometer (FT-IR), and N_2 adsorption–desorption techniques. The malachite green (MG) removal performance of the prepared AC was evaluated under various MG concentrations, pH, and MG/AC ratios. The porous AC shows a fully developed structure with a specific surface area (SSA) of 1900 m^2/g and a total pore volume ($V_{total\ pore}$) of 1.051 cm^3/g. MG could be efficiently removed from aqueous solutions by the prepared AC with rich pores and surface functional groups. MG adsorption capacity of 2209.07 mg/g was observed at the initial MG concentration of 500 mg/L. The MG adsorption mechanism by the prepared AC was explored through the adsorption kinetics, isotherms, and thermodynamics models. The adsorption results could be well illustrated by the pseudo-second-order kinetic model with a R^2 of 0.9990 and Langmuir isothermal model with a R^2 of 0.9830 indicating the chemisorption dominated in the homogeneous and monolayer adsorption. The diffusion of MG into AC is mainly controlled by the intraparticle diffusion. $\Delta G^0 < 0$ demonstrated the spontaneous nature of MG adsorption onto AC, and $\Delta H^0 > 0$ implied the endothermic nature of the adsorption process. This is the reason that the adsorption capacity was improved from 2464.10 to 2623.77 mg/g as the temperature was increased from 298 to 318 K at the same MG initial concentration. This work could provide some references to produce efficient adsorbents from biomass.

Keywords Pine sawdust · Hydrothermal treatment · KOH activation · Activated carbon · Malachite green

Introduction

Water pollution is one of the most hazardous industrial issues in such an urbanized and industrialized era [1, 2]. More than 100,000 dyes, which are the most representative organic water pollution, are extensively used in many industries such as textile and leather [3, 4]. Among them, malachite green (MG) is a typical triphenylmethane dye with severe toxicity and the most representativeness. It will cause a series of harmful influences on the living body if MG-contaminated water is discharged without treatment.

Consequently, the efficient separation and removal of MG have aroused widespread concerns.

Various methods and techniques, including adsorption [5–8], oxidation, precipitation, biochemical process, ion exchange, and photodegradation, have been proposed to remove dye from the wastewater. Since MG is water-soluble and difficult to photodegradation [9] and bio-degradation, adsorption exhibited the most promising for MG removal because of its simple, no secondary pollution, high efficiency, and convenient handling [10]. Commercial AC, commonly derived from coal, pitches, and coke, was used by many industries to deal with dye waste problems. However, it was not an economic feasible adsorbent due to its precursors are non-renewable and high-cost. Hence, to improve adsorption capacity and lower the cost, the alternative materials with high-production, widespread availability and renewability, and low-cost were studied by many researchers to replace the traditional coal-based materials.

Waste biomass is now regarded as a proper precursor for preparing AC adsorbents as an abundant carbon-rich

---

Xin Cui and Didi Gai contribute equally to this work.

✉ Peitao Zhao
p.zhao@cumt.edu.cn

[1] School of Low-Carbon Energy and Power Engineering, China University of Mining and Technology, Jiangsu, Xuzhou 221116, People's Republic of China

resource. Ren et al. [11] reported that the garlic root with rich hydroxyl and carboxyl groups showed good MG removal ability of 232.56 mg/g$_{absorbent}$. The amino groups on the brown marine algae surface significantly increased the adsorption capacity to 76.92 mg/g$_{adsorbent}$ at the pH of 10 [12]. Mullick and Neogi [1] prepared AC from stevia leaves by sodium hydroxide impregnating for MG removal. The adsorption capability was improved from 73.08 to 288.67 mg/g when the initial concentration increased from 50 to 300 mg/L. Pragathiswaran et al. [13] prepared the AC from *Gloriosa superba* stem to remove MG, and the removal efficiency of 90.5% was obtained at the initial concentration of 50 mg/L with 250 mg AC under the temperature of 30 °C and pH of 6.5.

AC is generally prepared by two steps: carbonization and activation. Both pyrolysis and hydrothermal carbonization are common carbonization technique. Pyrolysis was usually operated under high temperature, and the release of volatile would generate tar causing operating issues. Compared to pyrolysis, hydrothermal carbonization (HTC) is devoted to overcome the intensive energy consumption in drying process for moist biomass. It is performed at a milder reaction temperature of 180–250 °C, and the final products could be easily separated from reaction mixture. HTC is therefore widely accepted to be promising for converting moist biomass into hydrochar with good morphology, rich functional groups, and lower aromatization degree etc. [14–16]. Hydrochar has been widely applied in adsorption due to above advantages. Zhang et al. [17] prepared hydrochar using phycocyanin-extracted algal bloom residues (PE-ABR) and reported the PE-ABR hydrochar showed a maximum adsorption capacity of 89.05 mg/g for MG. After being pyrolyzed at 800 °C, the hydrochar from bamboo shoot shell (BHC-800) exhibited a surface area of 513 m^2/g and maximum RhB adsorption capacity of 85.8 mg/g [18]. The hydrochar derived from PVC and alkali coal had an adsorption capacity of 322.10 mg/g with a surface area of 20.578 m^2/g [19]. The adsorption capacity of hydrochar is generally low because of its low surface area and pore volume with less sorption sites for contaminants [20, 21].

Chemical activation was commonly utilized to improve the adsorption capacity of hydrochar. The activators usually included H$_3$PO$_4$, KOH, ZnCl$_2$, and K$_2$CO$_3$. The generated AC shows larger SSA because the activators could prevent the pore structure from tar blocking. The perlite activated by oxalic acid showed good adsorption of heavy metal ions with surface area increase after acid treatment [22]. Hayashi et al. [23] prepared lignin-based AC via chemical activation, and K$_2$CO$_3$ showed the best activation performance. The surface area of rice husk increased to 922.319 m^2/g after ZnCl$_2$ activation [24]. Gupta et al. [25] obtained a graphene porous structure by promoting carbon gas generation and carbon gasification at 850 °C with KOH activation. The major micropores resulted in a relatively high SSA and pore volume of 1710 m^2/g and 0.834 m^3/g, respectively.

This work focused on the fabrication of hydrochar precursors with rich surface functional groups to generate AC. The AC with high SSA and pore volume was obtained by combing the hydrothermal pretreatment with KOH activation. The physicochemical properties of AC were characterized by N$_2$ adsorption–desorption, FT-IR, and SEM. The AC performance was evaluated by removal MG from the aqueous solution. The adsorption capacity of AC was investigated under various initial MG concentration, solution pH, and AC dosage. The adsorption kinetics, adsorption thermodynamics, and isothermal adsorption were also investigated to reveal the adsorption mechanism of pine dust-based AC on MG. The study proposes a reference to waste biomass utilization and efficient adsorbents preparation.

Materials and methods

Materials

The pine sawdust (PS) sample was collected from a wood processing plant in Xuzhou, Jiangsu Province. The PS was rinsed with deionized water to remove impurities and then dried in a 105 °C oven to remove moisture. The dried PS was ground and sieved to 100 mesh (150 μm). Table 1 lists the proximate and ultimate analysis of PS.

Table 1 Proximate and ultimate analysis of PS and hydrochar

Sample	Proximate analysis (wt. %)				Ultimate analysis (wt. %)					Heating value	Yield
	M$_{ad}$	A$_d$	V$_d$	FC$_d$	C$_{daf}$	H$_{daf}$	O$_{daf}$^{b}	N$_{daf}$	S$_{daf}$	(MJ/kg)	(%)
PS	10.63	0.21	87.86	11.93	51.42	6.03	42.32	0.21	0.02	17.74	-
Hydrochar	3.49	0.48	58.02	41.50	70.66	5.05	24.09	0.20	-	27.61	61.70

A ash, *M* moisture, *V* volatile matter, *FC* fixed carbon, *ad* air-dried basis, *d* dried basis, *daf* dried and ash-free basis

[b]Calculated by difference

Preparation of PS-based AC

Hydrothermal carbonization

Five g of PS was mixed with 100 mL of deionized water and then transferred to an autoclave reactor after thorough stirring. The argon flow was introduced to exhaust the air before the hydrothermal experiments. The reaction temperature and soaking time were set to 240 °C and 30 min, respectively [26]. Thereafter, the reactor was cooled down to room temperature, and the solid product (noted as "hydrochar") was separated from the liquid and oven-dried at 105 ± 5 °C to remove moisture.

Activation of hydrochar

The hydrochar was mixed with KOH at the mass ratio of 1:2 and activated in a tube furnace at 800 °C for 90 min under N_2 atmosphere of 300 mL/min. After cooling to ambient temperature, hydrochar was washed via 0.1 mol/L hydrochloric acids and stirred in a water bath at 80 °C for 20 min. After that, the hydrochar was repeatedly washed with deionized water and then dried at 105 ± 5 °C for 24 h to obtain AC.

Adsorption experiments

The adsorption experiments were carried out to evaluate the adsorption capacity of AC for MG. A certain amount of AC was added to 50 mL MG solution with the initial concentration ranging from 100 mg/L to 700 mg/L. The mixture was oscillated at 130 rpm for 24 h at different temperatures for adsorption. After adsorption, the MG solution was filtered, and its concentration was measured by UV-1800PC spectrophotometer (Mapada, China) under the wavelength of 618 nm. The equilibrium adsorption capacity of AC for MG solution (q_e) and the removal rate of MG (R) could be calculated by formulas (1) and (2), respectively:

$$q_e = \frac{(C_0 - C_e) \times V}{W} \tag{1}$$

$$R = \frac{C_0 - C_e}{C_0} \times 100\% \tag{2}$$

where C_0 and C_e (mg/g) are the initial concentration and the adsorption equilibrium of MG, respectively. V is the volume of the solution (L), and W is the mass of AC (g).

Regeneration

The regeneration concluded adsorption and desorption processes. In the adsorption process, 40 mg AC was added into a 200 mL MG solution with initial concentration of 400 mg/L, and then the mixture was oscillated under the temperature of 298 K for 24 h. The used AC was collected for desorption experiment after washing and drying. Ten mL deionized water, HCl (0.1 mol/L), NaOH (0.1 mol/L), and absolute ethyl alcohol (CH_3CH_2OH) were used as desorption agent to react with 10 mg used AC, respectively. The desorption was performed under the room temperature for 3 h. The desorption amount and rate were calculated by the following formulas:

$$q_a = \frac{(C_0 - C_a)v_a}{W_a} \tag{3}$$

$$q_d = \frac{C_d v_d}{W_d} \tag{4}$$

$$D = \frac{q_d}{q_a} \times 100\% \tag{5}$$

where q, C, v, D, and W are standard for adsorption amount, MG concentration, solution volume, desorption rate, and adsorbent weight. The subscript 0, a, and d here represented the initial value of concentration, adsorption, and desorption.

In this study, the sample was characterized via FT-IR, N_2 adsorption–desorption, and SEM. Details on the AC preparation and characterization are listed in Supplementary Material.

Results and discussions

Characterization

Properties of PS and hydrochar

Compared to PS, the fixed carbon and volatile content in hydrochar changed with an increase of 29.57% and a decrease of 29.84% (Table 1) because of the removal of organic matters by hydrothermal treatment. The carbon content in hydrochar increased obviously with a rate of 19.24% due to the dehydration and decarboxylation reaction. Meanwhile, the heating value decreased for the reduction of cellulose and lignin. These results exhibited that the hydrochar derived from PS had been treated adequately.

TGA was applied to investigate the effect of hydrothermal pretreatment on PS (Fig. 1). For all samples, the first weightlessness peak of DTG curves concerning the temperature below 150 °C was ascribed to moisture loss. The largest and fastest weight loss peak of PS with a weight loss of about 40% was observed at 320 °C, which could be attributed to the decomposition of cellulose and hemicellulose. TG and DTG curves on hydrochar did not exhibit the

Fig. 1 TG/DTG curves of PS and hydrochar
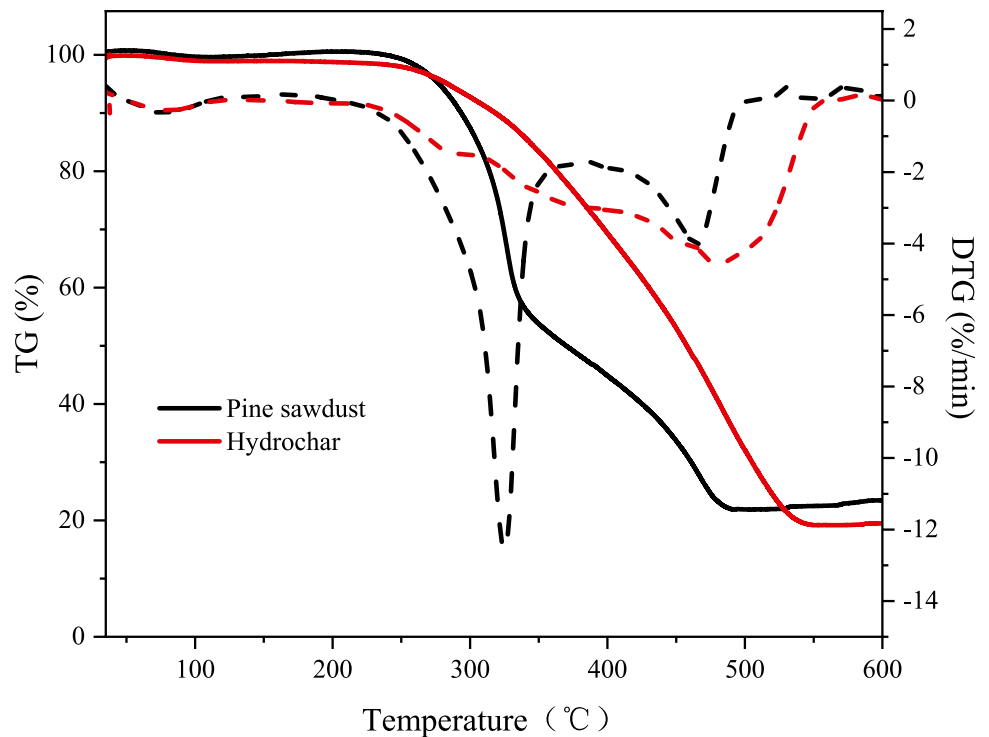
obvious weight loss change, implying that hydrothermal treatment under the temperature of 240 °C could remove most volatile matters in PS. The char and fixed carbon in the PS burned at the range of 370–500 °C, resulting the third weight loss peak of PS. However, the weightless peak of hydrochar was different from PS. Between 200 and 600 °C, the weight loss rate slowed down considerably due to the breakdown of larger lignin molecules. Meanwhile, the fixed carbon content increased, indicating that the hydrothermal pretreatment was favorable to subsequent chemical activation.

Surface morphology

The surface morphology and microstructure of fresh and pretreated PS samples could be appraised via the SEM graphs (Fig. 2). Figure 2a shows clear and slender fiber structure of the fresh PS with a smooth surface. The surface morphology of hydrochar (Fig. 2b) was rougher and more irregular due to the decomposition of glucan, cellulosic, and hemicellulosic sugars, as well as other organics during the hydrothermal process [27]. After activation, an obvious porous structure was generated via the KOH activation under
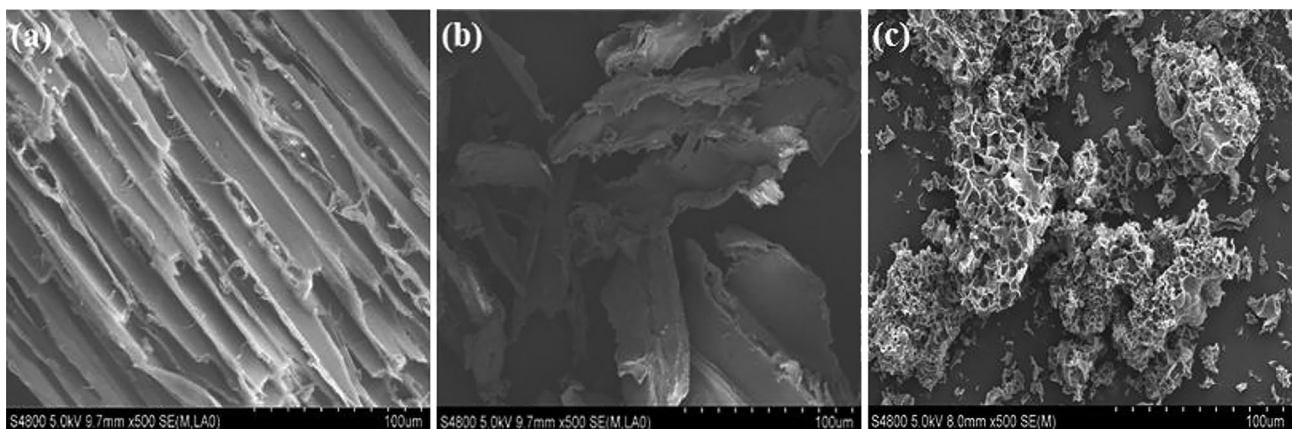

Fig. 2 SEM images of **a** PS; **b** hydrochar; and **c** AC

high temperature as depicted in Fig. 2c. The white particles on the surface of AC were attributed to the ash content in hydrochar (mainly SiO_2) which did not completely react with KOH. For comparison of these samples, hydrothermal pretreatment caused the organic macromolecule decomposition and the fiber wall breakdown of PS. Meanwhile, higher activation temperature and KOH impregnation promoted the chemical reactions between biomass and KOH by releasing gas, such as CO_2 and CO [25, 28]. A relatively high specific surface area could be expected according to these SEM graphs. Above all, the hydrothermal carbonization and KOH activation could promote the generation and development of porous structure of PS.

FT-IR analysis

As shown in Fig. 3, the infrared spectrum of hydrochar and AC exhibited stronger intensity, indicating the quantities of functional groups were enhanced after hydrothermal carbonization and chemical activation. All these materials showed strong peaks at 3416 cm^{-1}, which were attributed to the OH stretching vibration of hydroxyl functional groups. The peaks at 2921 cm^{-1} were assigned to the stretching vibration of C-H bonds, and the peak at 1617 cm^{-1} represented the stretching vibration of the C=C bonds in the benzene ring. The bands at 1427 cm^{-1} could be ascribed to an O–H deformation vibration in carboxyl groups [29]. Bands in the region of 1104–998 cm^{-1} showed the presence of C-O, which was ascribed to alcohols, phenols, acids, or esters [30]. The out-of-plane bending vibration of aromatic peak of C-H at 870 cm^{-1} and 711 cm^{-1} indicated the existence of aromatic ring structures. These peaks in the hydrochar are
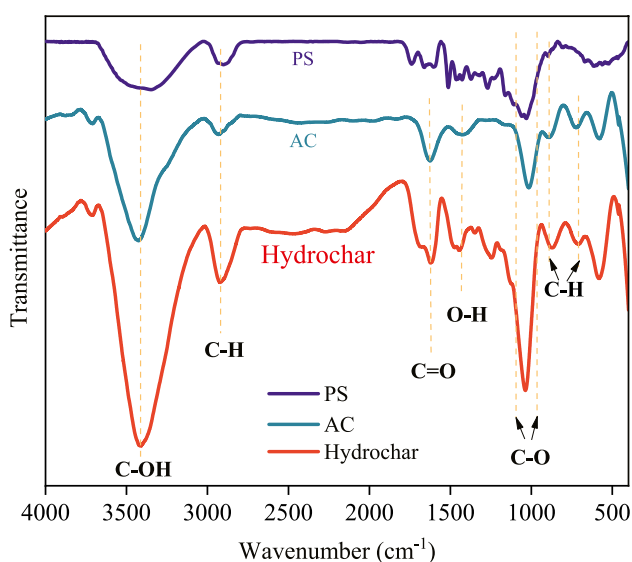
already strong enough compared with original PS samples as a consequence of the rearrangement and reorganization of original functional groups in PS [27]. The strength of most hydrochar surface functional groups decreased after activation, which was correlated to the products generating from these aryl-condensation, polymerization, and etherification reactions reacting with KOH at 800 °C [31]. The SEM and FT-IR revealed the introduction of various functional groups onto the AC surface. This might be beneficial to the MG adsorption because these surface functional groups could serve as the "active sites."

N₂ adsorption–desorption

The pore structures could be divided into macropores (>50 nm), mesopore (2–50 nm), and micropore (<2 nm). Figure 4a reveals that the pores of fresh PS and hydrochar were mainly distributed in the range of 4–8 nm, which belong to mesopores. As depicted in Fig. 4b, an obvious hysteresis loop could be observed in the isothermals of the hydrochar, convincing its apparent mesoporous structure. N_2 adsorption–desorption isotherms indicated the larger pores existed in the PS sample, which was consistent with its average pore size of 59.72 nm in Table 2. The hysteresis loops of PS and hydrochar isothermals can be regarded as the H3 type without an obvious saturated adsorption platform [32]. It implies the irregular pore structure with the presence of the slit-type pores which were accumulated by platelet particles. The isothermal of AC (Fig. 5a) corresponded to the type I curve (also known as *Langmuir* adsorption curve), standing for the typical microporous adsorption [32, 33]. The hysteresis loop was absent in the isothermal because of few mesopores existing in AC sample [34].

Table 2 displayed that the specific surface area (SSA) of PS was highly improved from 2.476 to 1900 m^2/g, and the total pore volume ($V_{pore\ volume}$) was increased from 0.036 to 1.051 cm^3/g after the combination of hydrothermal carbonization and KOH activation. HTC increased the SSA of PS by 24 times and the total pore volume by three times, and KOH activation induced the 767 times and 29 times SSA and $V_{pore\ volume}$ increment of PS, respectively. The average pore diameter of AC is 2.11 nm as shown in Table 2, suggesting that the macropores of PS were crushed into micropores and partial mesopores. The hydrolysis of cellulose and hemicellulose resulted in the generation of massive pores

Fig. 3 FT-IR spectra of PS, hydrochar, and AC

Table 2 Structural parameters of PS, hydrochar, and AC

Sample	SSA (m^2/g)	Total pore volume (cm^3/g)	Average pore diameter (nm)
PS	2.476	0.036	59.720
Hydrochar	60.190	0.109	7.276
AC	1990	1.051	2.111

Fig. 4 Pore structure characterization of fresh PS and hydrochar. **a** Pore width distribution circle, hydrochar; square, PS. **b** N_2 adsorption–desorption isotherms
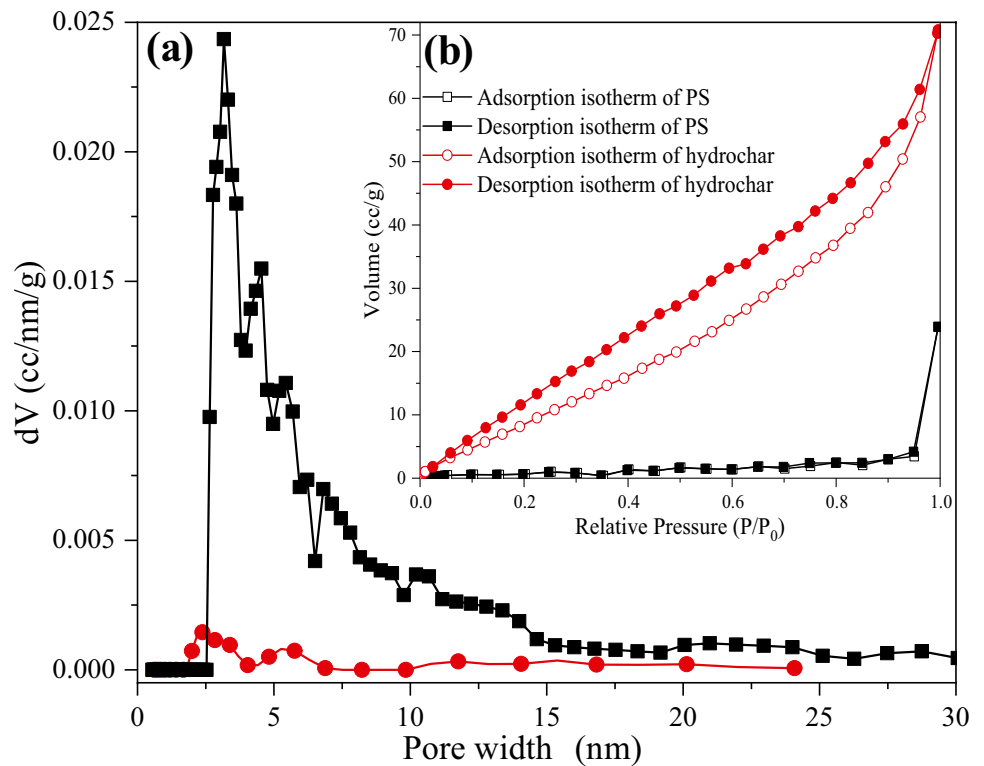
in hydrochar, and the carbon skeleton could develop a large number of micropores after KOH activation because of the redox reactions [35]. According to the previous work, the redox reaction on alkaline activation could be summarized as a global reaction in Eq. (6) [36]. The activator KOH could reacted with carbon causing the generation of K metal and

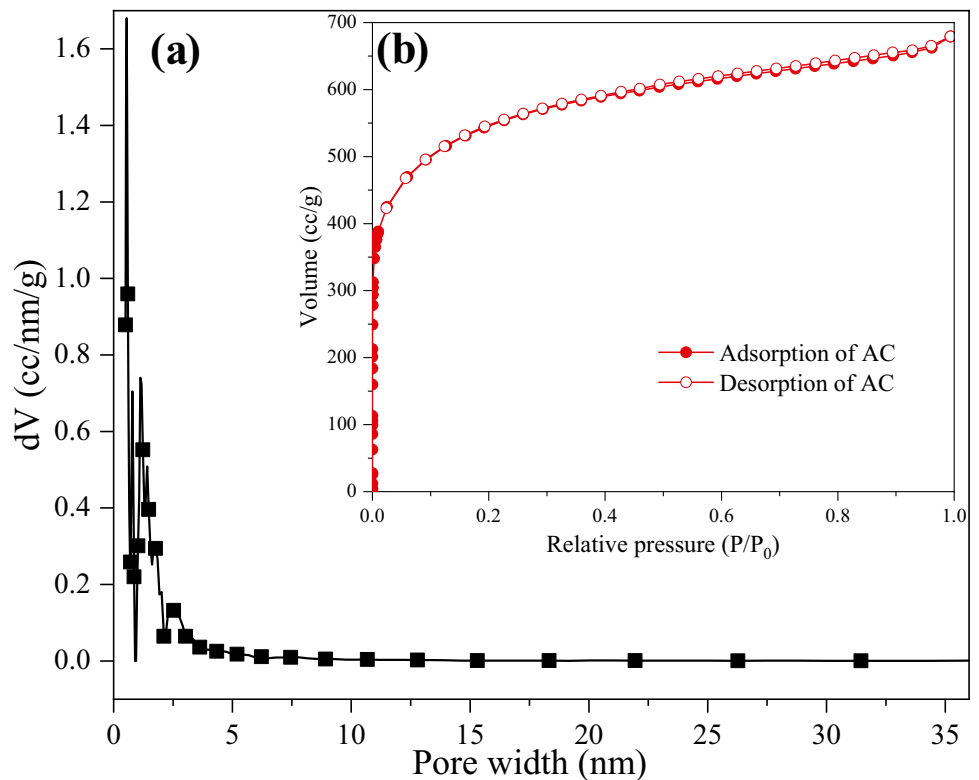**Fig. 5** Pore structure characterization of AC. **a** Pore width distribution. **b** Adsorption–desorption isotherms of N_2
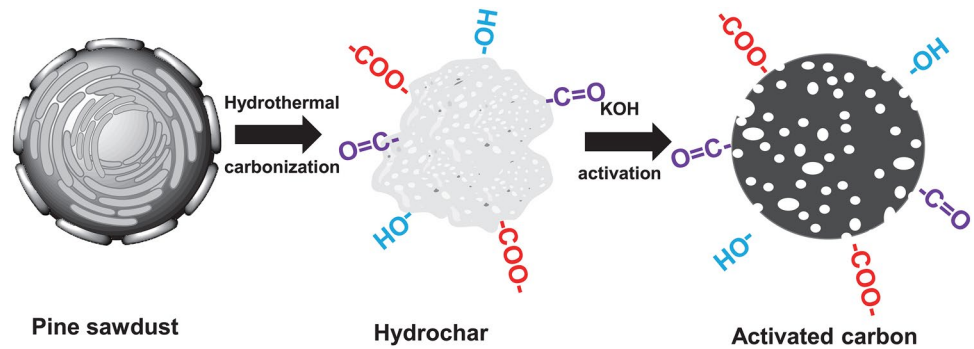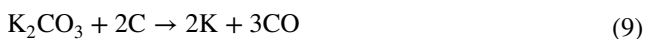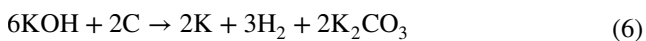
Fig. 6 The proposed mechanism of hydrothermal prefabricated of AC

Pine sawdust   Hydrochar   Activated carbon

K_2O. The produced K metal (Eqs. 7–10) [37] could be intercalated between the graphene layers of the hydrochar to separate the layers, which resulted in the irreversible enlargement of carbon lattice and favored the generation of micropores. Consequently, the SSA and pore volume were obviously facilitated after activation. Therefore, hydrothermal pretreatment and KOH activation are beneficial for developing the porous structure of PS:

$$6KOH + 2C \rightarrow 2K + 3H_2 + 2K_2CO_3 \qquad (6)$$

$$K_2CO_3 + C \rightarrow K_2O + 2CO \qquad (7)$$

$$K_2CO_3 \rightarrow K_2O + CO_2 \qquad (8)$$

$$K_2CO_3 + 2C \rightarrow 2K + 3CO \qquad (9)$$

$$C + K_2O \rightarrow 2K + CO \qquad (10)$$

Mechanism of hydrothermal prefabricated AC

Based on these characterizations, a reasonable mechanism is proposed for the formation of carbon skeleton and porous AC, involving two processes as presented in Fig. 6. The fibers, shown in SEM graphs of PS, are mainly composed of cellulose, hemicellulose, and lignin. They were converted into gas and liquid products containing H and O, and residual solid products contained a large part of carbon in hydrochar. The long and narrow smooth structure of PS was destroyed, and some pores were generated resulting from the release of tar and volatiles. The carbon skeleton was preliminarily constructed following with the removal of many weaker functional groups. The second process is pore formation due to chemical reagent etching. KOH activation is responsible to the development of pores. It was ascribed to be a redox reaction, and the potassium metal was inserted into the carbon layer to create more micropores and higher surface area. The total pore volume and specific surface area were highly enhanced according to the N2 adsorption and desorption test. The rich pores and functional groups are supposed to improve adsorption performance for MG removal.

## Influencing factors for adsorption capacity of AC

Effect of adsorbent dosage

The adsorbent dosage determined the number of active sites in the adsorption system, which remarkably affected the whole adsorption process. Five, 10, 15, 20, and 25 mg AC was weighed and then added to 50 mL MG solution with a concentration of 500 mg/L to investigate the effect of adsorbent dosage on MG removal. The adsorption was performed at 25 °C for 24 h under the mixing speed of 130 rpm. As shown in Fig. 7, the removal rate was increased as the increase of adsorbent dosage when the dosage was less than 15 mg. It could be attributed to the increase of adsorption sites during the adsorption process. The highest MG removal rate appeared as 99.90% at 15 mg and then stabilized with the rise of AC dosage. It indicated the AC adsorption was unsaturated when the AC addition was greater than or equal to 15 mg. Besides, the adsorption capacity of AC decreased from 2578.72 to 999.08 mg/g with the dosage. This is because the increment of adsorbent dosage did not match that of adsorption amount, resulting in lower adsorptive capacity utilization. Ten mg was set as an optimal adsorption dosage for economic and energy-saving considerations as the initial MG concentration of 500 mg/L in this study.

Effect of initial MG concentration

The initial concentration of MG dye can help to overcome the mass transfer limitation between the solid adsorbent and aqueous solution. Fifty mL MG solution with a concentration ranging from 100 to 700 mg/L was mixed with 10 mg AC under 25 °C for 24 h, respectively. Figure 8 depicts the MG could be completely removed when the MG concentration was lower than 300 mg/L. The lower concentration of MG solution (< 300 mg/L) has less adsorbate to completely

**Fig. 7** Effect of AC dosage on MG adsorption performance
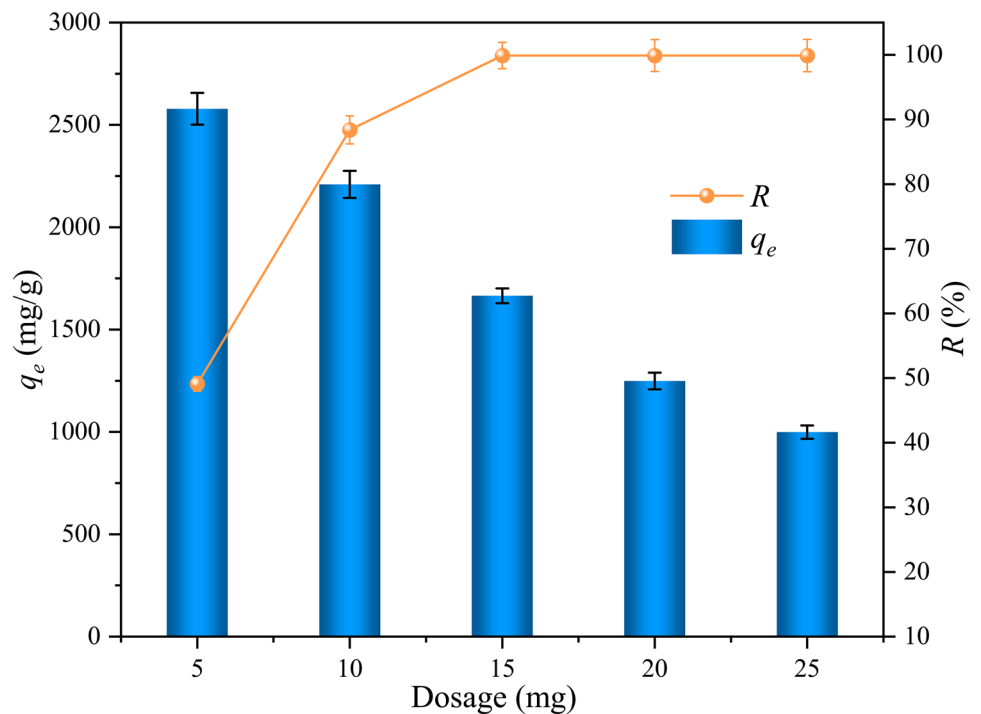
occupy the adsorption sites provided by 10 mg AC, so the removal efficiency can reach almost 99.9%.

The removal rate declined rapidly with the rise of MG concentration because the adsorbent offered a limited number of surface adsorption sites. The higher MG concentration exceeded the adsorption capacity of the adsorbent. As

the initial concentration increases, the adsorbate uptake is smaller than the increment of initial concentration, leading to the decrease of adsorption efficiency. Therefore, the adsorption sites were maintained saturated during the adsorption process when the initial concentration was more than 300 mg/L. This phenomenon was also known as the

Fig. 8 Effect of MG initial concentration on adsorption performance of AC
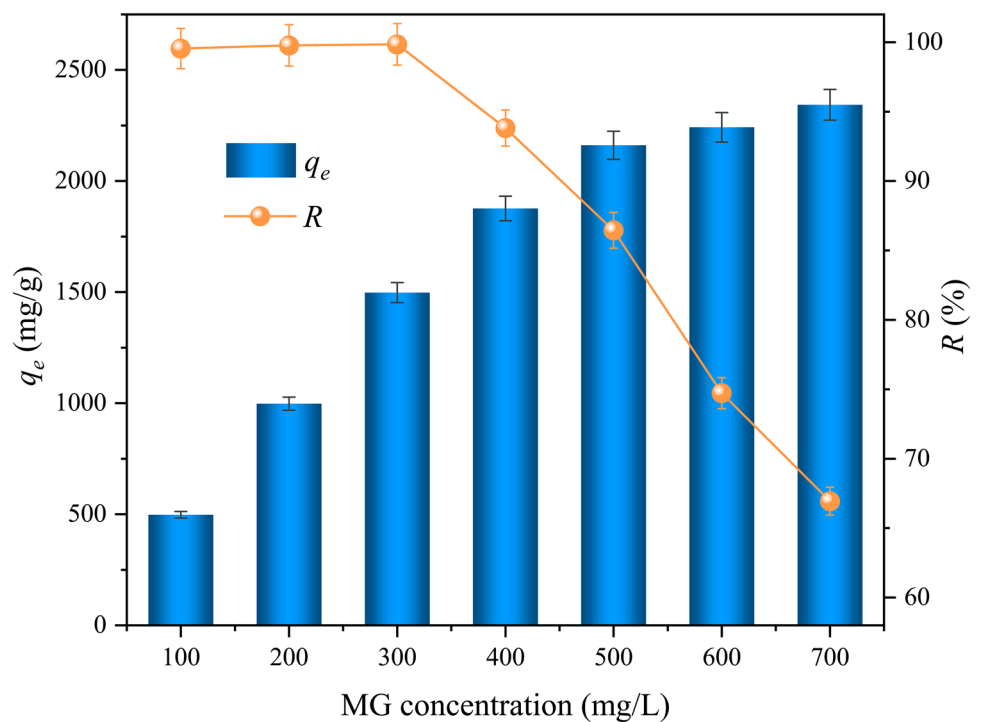
adsorbent concentration effect [38]. It could be seen clearly the q_e values increased with the initial MG concentration. This is because the high mass gradient resulted from the increase of initial concentration provided an important driving force for the migration of MG molecules onto AC [39]. Combined with the effect of equilibrium adsorption capacity and MG removal rate, 500 mg/L MG solution was selected as the experimental condition in the subsequent experiments.

Effect of initial pH

The pH of an aqueous solution played an important role in the adsorption process of MG via the physicochemical properties of adsorbents and adsorbates [40, 41]. The pH of the solution was adjusted to 2, 4, 6, 8, and 10, respectively, by HCl and NaOH, and the adsorbate (MG) was 50 mL. Figure 9 reveals that the equilibrium adsorption capacity q_e increased with the pH values. The lowest adsorption capacity of 1202.53 mg/g and efficiency of 48.1% occurred at a pH of 2, and it might be attributed to the ion competition between H^+ and $N(CH_3)$, known as electrostatic repulsion. The $N(CH_3)$ was obtained from MG dissociation because the MG acid dissociation constant (pKa = 10.3) showed that the surface functional groups of dye solutions were prone to protonation at lower pH values and were easily de-protonated at higher pH [42] in the pH range of 2.0–10.0. The increment of equilibrium adsorption capacity began to slow down when the pH was greater than 4. The removal rate increased with the increment of pH. The

polarity of the AC surface was affected by the electric double layer of the solution. The adsorption capacity q_e increased from 2001.18 mg/g at pH of 4 to 2495.45 mg/g at pH of 10. The MG removal rate increased from 80.0% at pH of 4 to a maximum of 99.81% at pH of 10. The increasing pH values are favorable to the generation of OH^- and the reduction of electrostatic repulsion. At alkaline environment (pH > 7), the electrostatic force between OH^- and $N(CH_3)$ greatly facilitated the adsorption process. This observation was consistent with the report of Qu et al. [43]. Therefore, the pH value could affect the removal rate and equilibrium adsorption capacity of MG. The electrostatic force might be one of the main adsorption mechanisms. All the following experiments were carried out at the initial solution pH of 6 considering the characteristics of solution itself and the effect of solution pH on AC adsorption performance.
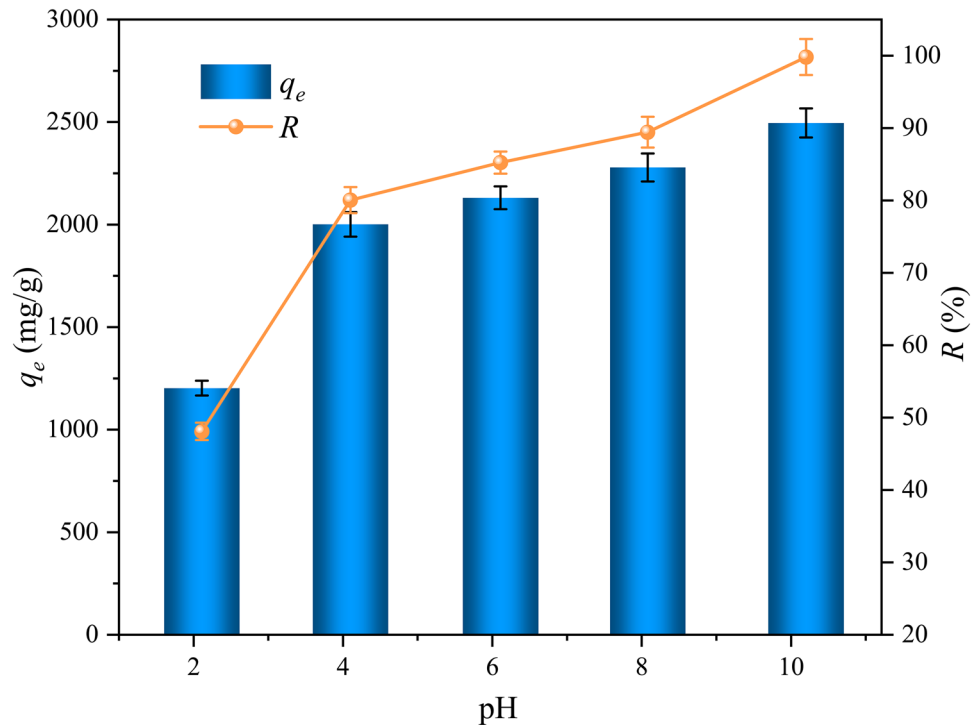
Adsorption models

Adsorption kinetics

The pseudo-first-order (PFO) and pseudo-second-order (PSO) equations were applied to study the relationship between the adsorption equilibrium time and the adsorption rate. The pseudo-first-order equations [44] are described as Eqs. (11) and (12):

$$\ln(q_e - q_\tau) = \ln q - k_1 \tau \tag{11}$$

Fig. 9 Effect of solution pH on adsorption performance of AC

$$q_\tau = q_e\left(1 - e^{-k_1\tau}\right) \tag{12}$$

where q_e and q_τ are the amounts of MG adsorbed per mass of adsorbent at equilibrium (mg/g) and at time τ (mg/g), respectively, and k_1 is the adsorption rate constant (min^{-1}). The values of k_1 and q_e were derived from the slopes and intercepts of the fitted nonlinear equation.

The linear and nonlinear forms of the pseudo-second-order equations based on equilibrium adsorption [45] are expressed as follows:

$$\frac{t}{q_\tau} = \frac{1}{k_2 q_e^2} + \frac{1}{q_e}\tau \tag{13}$$

$$q_\tau = \frac{q_e^2 k_2 \tau}{1 + q_e k_2 \tau} \tag{14}$$

where k_2 is the adsorption rate constant of PSO (g/mg·min). Meanwhile, k_2 and q_e were obtained from the slope and intercept of the plot $\frac{q_\tau}{\tau}$ versus τ.

The kinetic studies were performed using the curve fitting tools provided in Origin Pro 2018. The error functions that were used to optimize the model were listed as follows [46] :

$$R^2 = 1 - \frac{\sum_{i=1}^{n}\left(q_{e,\exp} - q_{e,cal}\right)^2}{\sum_{i=1}^{n}\left(q_{e,\exp} - \overline{q}_{e,cal}\right)^2} \tag{15}$$

$$RMSE = \sqrt{\frac{1}{N-2} \times \sum_{i=1}^{N}\left(q_{e,\exp} - q_{e,cal}\right)^2} \tag{16}$$

Figure 10 shows the AC intake speed had a rapid increase at 120 min and 480 min for the solutions with an initial concentration of 300 mg/L and 500 mg/L at 298 K, respectively. Thereafter, the adsorption increment of AC slowed down until stable. For 300 mg/L solution after 24 h reaction, the final adsorption amount of AC was 1497.71 mg/g, and the removal rate was up to 99.84%, indicating the completeness of the adsorption. The adsorption capacity of 2209.07 mg/g was observed at the MG concentration of 500 mg/L, resulting in a removal rate of 88.36%. The higher removal rate and capacity were observed at the 500 mg/L MG solution because the higher MG concentration could strengthen the mass transfer, resulting in more MG molecules absorbing on active sites of the AC surface [47]. The adsorption kinetics parameters were presented in Table 3. The fitting results indicated that the kinetic models could fit well with experimental results because all R^2 are above 0.9. Although the q_e from PFO model was close to the experimental value as shown in Fig. 10a, the lower R^2 of PFO indicated the adsorption of MG on AC matched better with the PSO model. To better describe the kinetic fitting results, *RMSE* error analysis was applied, and the lower error function values corresponded to the coefficient of determination. Baek et al. [48] obtained the same kinetic fitting results for the adsorption of MG on defatted coffee beans.

The intraparticle diffusion (ID) model considering both the membrane diffusion process and the intraparticle diffusion process as shown in Eq. (17) was applied to further investigate the diffusion modes during the adsorption process:

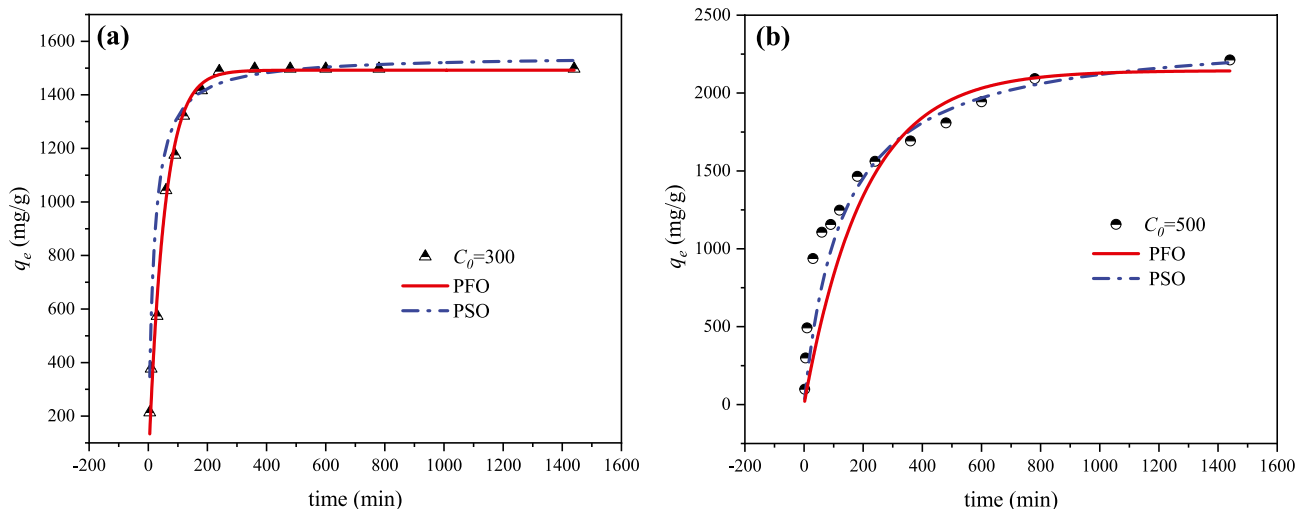$$q_\tau = k_i \tau^{\frac{1}{2}} + c \tag{17}$$

Fig. 10 PFO and PSO kinetics for adsorption of MG with initial concentrations of **a** 300 mg/L and **b** 500 mg/L (T = 298 K, adsorbent = 0.2 g, V = 0.1 L)

Table 3 Adsorption kinetic parameters of MG on AC

Kinetics	Parameters	Initial MG concentrations	
		300 mg/L	500 mg/L
PFO	$q_{e,exp}$ (mg/g)	1497.71	2209.07
	$q_{e,cal}$ (mg/g)	1492.06	2143.90
	k_1 (min^{-1})	0.018	0.005
	R^2 (nonlinear)	0.988	0.996
	RMSE	20.451	49.357
PSO	$q_{e,cal}$ (mg/g)	1546.90	2392.57
	$k_2 \times 10^3$ (g/mg·min)	0.037	0.003
	R^2 (nonlinear)	0.999	0.999
ID	$K_{i,1}$ (mg/g min$^{0.5}$)	125.40	208.56
	RMSE	15.688	47.678
	c_1	154.56	−176.12
	R^2 (linear)	0.947	0.995
	$K_{i,2}$ (mg/g min$^{0.5}$)	-	41.92
	RMSE	78.994	-
	c_2	-	827.89
	R^2 (linear)	-	0.934
	RMSE	-	69.988

where k_i represents the intraparticle diffusion rate constant (mg/(g·min$^{1/2}$)) and c reveals the effects of the boundary layer on the adsorption rate which is proportional to the boundary layer thickness. Figure 11b depicted that there were two sections in the fitted plots, revealing both the intraparticle and membrane diffusion existed in the adsorption process [49]. The first section with a larger slope corresponded to the membrane diffusion, implying the dispersion of MG molecules from the solution onto the AC surface. The

second section with a smaller slope was intraparticle diffusion, representing the migration of MG molecules from the AC surface to the internal pores. Consequently, at the beginning of the adsorption process, MG molecules diffused from the liquid phase to the surface of AC. With the decrease of MG concentration in the solution, the intraparticle diffusion dominated the MG removal rate.

Adsorption isotherms

Adsorption isotherms were applied to explore the interactions between the adsorbents and adsorbates and the distribution of solutes between solid and liquid phases. The reaction mechanism of the adsorption system could be deduced by some theoretical or empirical models. The Langmuir and Freundlich isotherms were widely used to study the relationship between the adsorption capacity and the equilibrium concentration of adsorbate under a certain temperature [50]. The Langmuir equation was expressed as following:

$$q_e = \frac{q_m K_L C_e}{1 + K_L C_e} \tag{18}$$

$$\frac{C_e}{q_e} = \frac{1}{q_m K_L} + \frac{C_e}{q_m} \tag{19}$$

where q_m (mg/g) is the theoretical monolayer saturated adsorption capacity, C_e (mg/L) is the adsorption equilibrium concentration, and K_L is the Langmuir constant related to the adsorption capacity of AC. Higher K_L value represents the stronger relationships between the MG molecules and AC.

A dimensionless parameter is proposed by Hall et al. for a more intuitive and convenient understanding of the
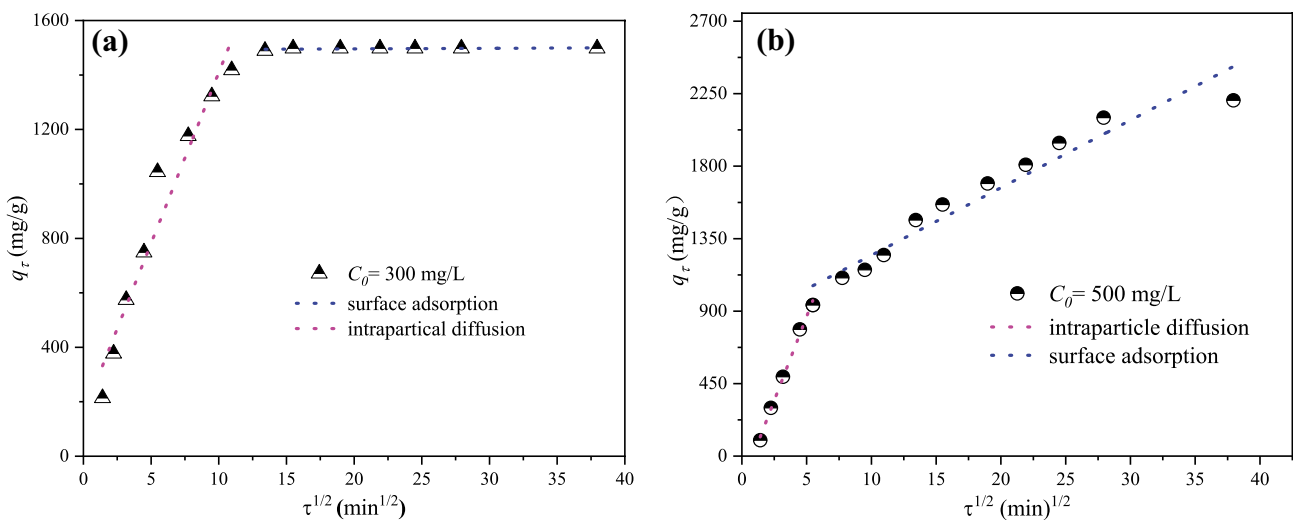

Fig. 11 ID for AC on MG with the initial concentration of **a** 300 mg/L and **b** 500 mg/L (T = 298 K, adsorbent = 0.2 g, V = 0.1 L)

mechanisms revealed by the Langmuir model [51]. The specific expression of R_L was

$$R_L = \frac{1}{\left(1 + K_L C_0\right)} \tag{20}$$

where C_0 is the maximum initial concentration (mg/L). The different values of R_L represent different types of adsorption such as disadvantageous ($R_L > 1$), advantageous ($R_L < 1$), and linear ($R_L = 1$) [52].

The Freundlich equation was regarded as an empirical model to describe the sorption occurring on the surface of heterogeneous adsorbate, which was applicable for multilayer adsorption with uniform and reversible energy. The linear and nonlinear forms are given by the following equations [53]:

$$q_e = K_F C_e^{\frac{1}{n}} \tag{21}$$

$$\ln q_e = \ln K_F + \frac{1}{n}\ln C_e \tag{22}$$

where K_F (mg/g·(L/mg)$^{1/n}$) represents the Freundlich sorption equilibrium rate and n is the indicator of adsorption strength. The interaction between adsorbent and adsorbate increases with the value of n. The adsorption reaction is easy to happen as $n > 1$, and the Freundlich model can be simplified to a linear model as $n = 1$.

The isothermal adsorption process was conducted at the temperature of 298 K, 308 K, and 318 K. Figure 12 depicts that the AC adsorption capacity increased with the initial MG concentration and the experimental temperature, revealing that the adsorption process was an endothermic reaction. The adsorption capacity of MG on AC was as
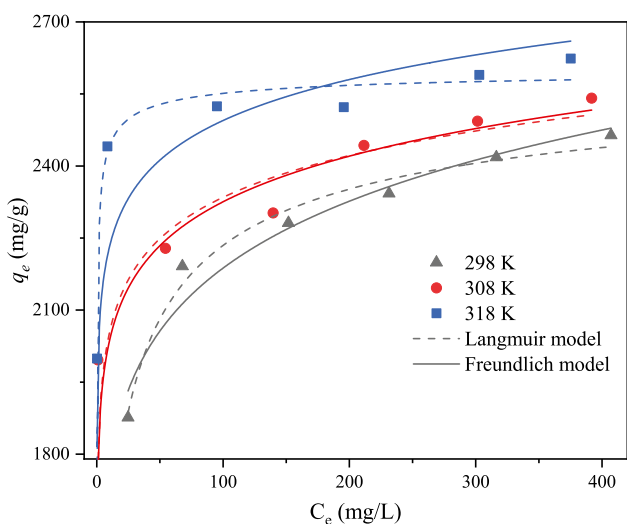
Table 4 Isothermal adsorption fitting parameters of MG on AC

Isotherms	Parameters	Activated carbon		
		298 K	308 K	318 K
Langmuir	q_m (mg/g)	2641.040	5403.438	2614.104
	K_L (L/mg)	0.409	0.493	4.910
	R_L	0.00272	0.00225	0.00023
	R^2	0.983	0.871	0.875
Freundlich	K_F (mg/g(L/mg)$^{1/n}$)	1451.491	1781.952	1995.257
	n	11.228	17.299	20.613
	R^2	0.957	0.871	0.814

high as 2623.77 mg/g at the MG initial concentration of 900 mg/L at 318 K. Table 4 shows the parameters from the fitting with these two isotherms models. The correlation coefficient R^2 of the Langmuir model was higher than that of the Freundlich model, indicating the Langmuir model matched better for the adsorption process. The isothermal curves plotted in Fig. 12 also suggested that the Langmuir model well represented the experimental data at different temperatures. According to the Langmuir model assumptions, the adsorption of AC on MG was monolayer and uniform. The adsorption only occurred at specific adsorption sites, and MG molecules did not migrate on the AC surface
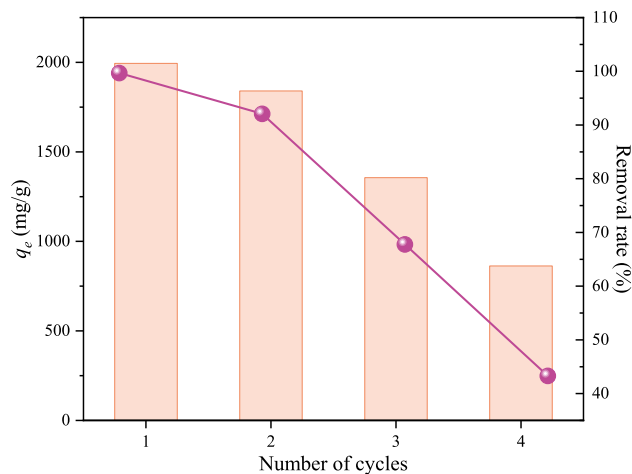
Fig. 12 Isothermal adsorption curves of MG on AC at 298, 308, and 318 K

Fig. 13 Chemical regeneration characteristics of AC for MG adsorption

Table 5 Thermal parameters of MG adsorption on AC

Temperature (K)	$\ln K^0$	ΔG^0 (kJ/mol)	ΔH^0 (kJ/mol)	ΔS^0 (kJ/mol/K)	R^2
298	3.997	−9.905	102.0	0.376	0.98452
308	5.657	−14.487			
318	6.594	−17.434			

Table 6 Comparison of MG adsorption capacity on different biomass-based adsorbents

Adsorbents	SSA (m²/g)	Activating agents	Isothermal model	Dosage (mg)	q_m (mg/g)	Reference
Pinus roxburghii cone AC	202	Acetic acid	Langmuir	20	250	[57]
Stevia leaves AC	281.8	NaOH	Freundlich	100	288.67	[1]
Textile sludge and sawdust AC (M6)	979	H_3PO_4	Langmuir	/	395	[58]
Yarn processing sludge AC2	1037	KI and KOH	Langmuir and Redlich–Peterson	50	498	[59]
Coconut Shell AC	1118.7	-	-	100	50	[60]
Elaeagnus angustifolia seeds AC	1194	H_3PO_4	Langmuir	100	115	[61]
Commercial coconut AC	1101	HF and HCl	Langmuir	50	91.24	[43]
Pine sawdust AC	1900	KOH	Langmuir	10	2209.07	This work

[43]. The chemical adsorption dominated the adsorption process [52], and the MG removal rate was limited by the internal diffusion of MG molecules [54].

Adsorption thermodynamics

The adsorption thermodynamics were applied to predict the thermodynamic mechanism under different conditions. Thermodynamic parameters in the adsorption process were calculated by the following formulas:

$$\Delta G^0 = -RT\ln K^0 \tag{23}$$

$$\ln K^0 = -\frac{\Delta H^0}{RT} + \frac{\Delta S^0}{R} \tag{24}$$

where ΔG^0, R, T, K^0, ΔH^0, and ΔS^0 represented criterion Gibbs energy (kJ/mol), gas constant (8.314 J/mol·K), thermodynamic temperature (K), Langmuir adsorption constant, standard adsorption enthalpy (kJ/mol·K), and entropy (kJ/mol), respectively.

The negative value of ΔG^0 in Table 5 confirmed the spontaneous nature of the adsorption process of MG by AC. The rising absolute value of ΔG^0 with the thermodynamic temperature manifested that the adsorption reaction was more likely to occur at higher temperatures. $\Delta H^0 > 0$ represented that the adsorption was an endothermic process. The enthalpy variation was above 40 kJ/mol, implying that the chemisorption dominated the adsorption process [55]. The positive value of ΔS^0 showed the ascending randomness of the solid–liquid interface and the strong affinity between MG molecules and the AC surface. The comparisons of the values of ΔH^0 and $T\Delta S^0$ confirmed the MG adsorption on the AC was mainly an entropy-controlled process [56].

Various biomass-based AC were listed in Table 6 to compare with the PS-based AC in this work. The maximum adsorption capacities and specific surface area of the prepared PS-based AC for the MG removal were found to be higher than that of other biomass-based AC. Most MG adsorption processes in Table 6 fitted well with Langmuir isothermal models. The PS-based AC showed the best adsorption performance with the fewer adsorbent dosage. This comparison further gave a support that the hydrothermal prefabricated AC derived from PS is an efficient and economic adsorbent for wastewater treatment.

Regeneration

Four desorption agents were applied in spent AC regeneration (Table S1). The highest desorption rate of 6.52% was observed in CH_3CH_2OH, demonstrating that the dominant adsorption way was chemisorption. CH_3CH_2OH was chosen to be desorption agent in the regeneration study. After four circle experiments, the adsorption capacity decreased from 1992.6 mg/g to 863 mg/g with a removal rate of 43.3% as shown in Fig. 13. These results showed that the PS-based AC could not realize the good durability and regeneration ability. Therefore, more attention could be paid to improving adsorbent stability.

Conclusions

The porous carbonaceous materials AC with excellent adsorption performance were prepared to remove MG from aqueous solutions. The basic carbon skeleton structure of AC was formed by hydrothermal prefabrication. The AC was endowed with good pore structure to be used as adsorbent due to its high SSA (SSA = 1900 m²/g) and total pore volume ($V_{total pore}$ = 1.051cm³/g) from KOH activation. The adsorption equilibrium occurred at the MG concentration of 300 mg/L, adsorbent dosage of 15 mg, and solution pH of 6. The PSO model could well describe the kinetic behaviors of adsorption. The highest adsorption capacity reached 2623.77 mg/g at 318 K at the initial concentration of 900 mg/L. Intraparticle diffusion became the main rate-limiting step with the decrease

of MG concentration in the solution. The better fitting result of the Langmuir model indicated that the MG adsorption on AC was monolayer and chemisorption process. The MG adsorption on AC is an entropy-driven endothermic process, and the increasing temperature is conducive to the adsorption. The excellent performance made AC a potential low-cost and convenient material for the efficient removal of MG. This work proposed a referential way to prepare porous adsorbents from waste biomass with low-cost, and further work could focus on the improvement of AC stability.

Declarations

Conflict of interest The authors declare no competing interests.

References

1. Mullick A, Neogi S (2016) Synthesis of potential biosorbent from used stevia leaves and its application for malachite green removal from aqueous solution: kinetics, isotherm and regeneration studies. RSC Adv 6:65960–65975. https://doi.org/10.1039/c6ra15225b

2. Song M, Wei Y, Cai S, Yu L, Zhong Z, Jin B (2018) Study on adsorption properties and mechanism of Pb^{2+} with different carbon based adsorbents. Sci Total Environ 618:1416–1422. https://doi.org/10.1016/j.scitotenv.2017.09.268

3. Zhang J, Zhao Y, Wu S, Jia G, Cui X, Zhao P et al (2022) Enhanced adsorption of malachite green on hydroxyl functionalized coal: behaviors and mechanisms. Process Saf Environ Prot 163:48–57. https://doi.org/10.1016/j.psep.2022.04.072

4. Tewari K, Singhal G, Arya RK (2018) Adsorption removal of malachite green dye from aqueous solution. Rev Chem Eng 34:427–453. https://doi.org/10.1515/revce-2016-0041

5. Zhou YM, Min YH, Qiao H, Huang Q, Wang EZ, Ma TS (2015) Improved removal of malachite green from aqueous solution using chemically modified cellulose by anhydride. Int J Bio Macromol 74:271–277

6. Rajabi M, Mirza B, Mahanpoor K, Mirjalili M, Najafi F, Moradi O et al (2016) Adsorption of malachite green from aqueous solution by carboxylate group functionalized multi-walled carbon nanotubes: determination of equilibrium and kinetics parameters. J Ind Eng Chem 34:130–138. https://doi.org/10.1016/j.jiec.2015.11.001

7. Yu J, Zhang LR, Liu B (2019) Adsorption of malachite green with sodium dodecylbenzene sulfonate modified sepiolite: characterization, adsorption performance and regeneration. Int J Env Res Public Health 16. https://doi.org/10.3390/ijerph16183297

8. Adebayo MA, Adebomi JI, Abe TO, Areo FI (2020) Removal of aqueous Congo red and malachite green using ackee apple seed–bentonite composite. Colloid Interfac Sci 38. https://doi.org/10.1016/j.colcom.2020.100311

9. Zhang MM, Mao YP, Wang WL, Yang SX, Song ZL, Zhao XQ (2016) Coal fly ash/CoFe2O4 composites: a magnetic adsorbent for the removal of malachite green from aqueous solution. RSC Adv 6:93564–93574. https://doi.org/10.1039/c6ra08939a

10. Chabane L, Cheknane B, Zermane F, Bouras O, Baudu M (2017) Synthesis and characterization of reinforced hybrid porous beads: application to the adsorption of malachite green in aqueous solution. Chem Eng Res Des 120:291–302. https://doi.org/10.1016/j.cherd.2016.12.014

11. Ren HJ, Zhang RN, Wang QC, Pan HY, Wang Y (2016) Garlic root biomass as novel biosorbents for malachite green removal: parameter optimization, process kinetics and toxicity test. Chem Res Chinese U 32:647–654. https://doi.org/10.1007/s40242-016-6095-5

12. Jerold M, Sivasubramanian V (2016) Biosorption of malachite green from aqueous solution using brown marine macro algae Sargassum swartzii. Desalin Water Treat 57:25288–25300. https://doi.org/10.1080/19443994.2016.1156582

13. Pragathiswaran C, Krishnan NA, Abbubakkar BM, Govindhan P, Abuthahir KS (2016) Kinetics and thermodynamics study of malachite green dye onto activated carbon obtained from the Gloriosa superba stem. Int J Res Pharm Chem 6:62–67

14. Lima HHC, Maniezzo RS, Llop MEG, Kupfer VL, Arroyo PA, Guilherme MR et al (2019) Synthesis and characterization of pecan nutshell-based adsorbent with high specific area and high methylene blue adsorption capacity. J Mol Liq 276:570–576. https://doi.org/10.1016/j.molliq.2018.12.010

15. Roman S, Nabais JMV, Ledesma B, Gonzalez JF, Laginhas C, Titirici MM (2013) Production of low-cost adsorbents with tunable surface chemistry by conjunction of hydrothermal carbonization and activation processes. Microporous Mesoporous Mater 165:127–133. https://doi.org/10.1016/j.micromeso.2012.08.006

16. Wang TF, Zhai YB, Zhu Y, Li CT, Zeng GM (2018) A review of the hydrothermal carbonization of biomass waste for hydrochar formation: process conditions, fundamentals, and physicochemical properties. Renewable Sustainable Energy Rev 90:223–247. https://doi.org/10.1016/j.rser.2018.03.071

17. Zhang H, Zhang FY, Huang Q (2017) Highly effective removal of malachite green from aqueous solution by hydrochar derived from phycocyanin-extracted algal bloom residues through hydrothermal carbonization. RSC Adv 7:5790–5799. https://doi.org/10.1039/c6ra27782a

18. Hou YR, Huang GG, Li JH, Yang QP, Huang SR, Cai JJ (2019) Hydrothermal conversion of bamboo shoot shell to biochar: preliminary studies of adsorption equilibrium and kinetics for rhodamine B removal. J Anal Appl Pyrolysis 143. https://doi.org/10.1016/j.jaap.2019.104694

19. Zhao P, Lin C, Li Y, Wu S, Cui X, Ding Y et al (2021) Value-added products from pyrolysis of hydrochar derived from polyvinyl chloride and alkali coal. J Cleaner Prod 329. https://doi.org/10.1016/j.jclepro.2021.129769

20. Fang J, Zhan L, Ok YS, Gao B (2018) Minireview of potential applications of hydrochar derived from hydrothermal carbonization of biomass. J Ind Eng Chem 57:15–21. https://doi.org/10.1016/j.jiec.2017.08.026

21. Xu QY, Liu TZ, Li L, Liu BY, Wang XD, Zhang SY et al (2021) Hydrothermal carbonization of distillers grains with clay minerals for enhanced adsorption of phosphate and methylene blue. Bioresour Technol 340. https://doi.org/10.1016/j.biortech.2021.125725

22. Ates A, Altintig E, Demirel H, Yilmaz M (2017) Comparative study on adsorptive removal of Cu, Pb, Zn heavy metals by modified perlite composites. Desalin Water Treat 98:244–253. https://doi.org/10.5004/dwt.2017.21671

23. Ji H, Kazehaya A, Muroyama K, Watkinson AP (2000) Preparation of activated carbon from lignin by chemical activation. Carbon 38:1873–1878. https://doi.org/10.1016/S0008-6223(00)00027-0

24. Altintig E, Acar I, Altundag H, Ozyildirim O (2015) Production of activated carbon from rice husk to support Zn^{2+} ions. Fresenius Environ Bull 24:1499–1506

25. Gupta K, Gupta D, Khatri OP (2019) Graphene-like porous carbon nanostructure from Bengal gram bean husk and its application for fast and efficient adsorption of organic dyes. Appl Surf Sci 476:647–657. https://doi.org/10.1016/j.apsusc.2019.01.138

26. Li JW, Zhao PT, Li T, Lei M, Yan WJ, Ge SF (2020) Pyrolysis behavior of hydrochar from hydrothermal carbonization of pinewood sawdust. J Anal Appl Pyrolysis 146: 104771. https://doi.org/10.1016/j.jaap.2020.104771

27. Wu Q, Yu ST, Hao NJ, Wells T, Meng XZ, Li M et al (2017) Characterization of products from hydrothermal carbonization of pine. Bioresour Technol 244:78–83. https://doi.org/10.1016/j.biortech.2017.07.138

28. Song M, Jin B, Xiao R, Yang L, Wu Y, Zhong Z et al (2013) The comparison of two activation techniques to prepare activated carbon from corn cob. Biomass Bioenergy 48:250–256. https://doi.org/10.1016/j.biombioe.2012.11.007

29. Moreno-Castilla C, Lopez-Ramon MV, Carrasco-Marin F (2000) Changes in surface chemistry of activated carbons by wet oxidation. Carbon 38:1995–2001. https://doi.org/10.1016/S0008-6223(00)00048-8

30. Zheng JY, Zhao QL, Ye ZF (2014) Preparation and characterization of activated carbon fiber (ACF) from cotton woven waste. Appl Surf Sci 299:86–91. https://doi.org/10.1016/j.apsusc.2014.01.190

31. Li M, Li W, Liu S (2011) Hydrothermal synthesis, characterization, and KOH activation of carbon spheres from glucose. Carbohydr Res 346:999–1004. https://doi.org/10.1016/j.carres.2011.03.020

32. Sing KSW (1985) Reporting physisorption data for gas/solid systems with special reference to the determination of surface area and porosity (Recommendations 1984). Pure Appl Chem 57:603–619. https://doi.org/10.1351/pac198557040603

33. Oginni O, Singh K, Oporto G, Dawson-Andoh B, McDonald L, Sabolsky E (2019) Influence of one-step and two-step KOH activation on activated carbon characteristics. Bioresour Technol Rep 7. https://doi.org/10.1016/j.biteb.2019.100266

34. Puthusseri D, Aravindan V, Madhavi S, Ogale S (2014) 3D micro-porous conducting carbon beehive by single step polymer carbonization for high performance supercapacitors: the magic of in situ porogen formation. Energy Environ Sci 7:728–735. https://doi.org/10.1039/c3ee42551g

35. Huang G, Liu Y, Wu X, Cai J (2019) Activated carbons prepared by the KOH activation of a hydrochar from garlic peel and their CO_2 adsorption performance. New Carbon Mater 34:247–257. https://doi.org/10.1016/s1872-5805(19)60014-4

36. Romanos J, Beckner M, Rash T, Firlej L, Kuchta B, Yu P et al (2012) Nanospace engineering of KOH activated carbon. Nanotechnology 23:015401. https://doi.org/10.1088/0957-4484/23/1/015401

37. Raymundo-Piñero E, Azaïs P, Cacciaguerra T, Cazorla-Amorós D, Linares-Solano A, Béguin F (2005) KOH and NaOH activation mechanisms of multiwalled carbon nanotubes with different structural organisation. Carbon 43:786–795. https://doi.org/10.1016/j.carbon.2004.11.005

38. Lin K, Pan J, Chen Y, Cheng R, Xu X (2009) Study the adsorption of phenol from aqueous solution on hydroxyapatite nanopowders. J Hazard Mater 161:231–240. https://doi.org/10.1016/j.jhazmat.2008.03.076

39. Auta M, Hameed BH (2012) Modified mesoporous clay adsorbent for adsorption isotherm and kinetics of methylene blue. Chem Eng J 198–199:219–227. https://doi.org/10.1016/j.cej.2012.05.075

40. Wang S, Zhu ZH, Coomes A, Haghseresht F, Lu GQ (2005) The physical and surface chemical characteristics of activated carbons and the adsorption of methylene blue from wastewater. J Colloid Interface Sci 284:440–446. https://doi.org/10.1016/j.jcis.2004.10.050

41. Saha P, Chowdhury S, Gupta S, Kumar I (2010) Insight into adsorption equilibrium, kinetics and thermodynamics of malachite green onto clayey soil of Indian origin. Chem Eng J 165:874–882. https://doi.org/10.1016/j.cej.2010.10.048

42. Mittal A (2006) Adsorption kinetics of removal of a toxic dye, malachite green, from wastewater by using hen feathers. J Hazard Mater 133:196–202. https://doi.org/10.1016/j.jhazmat.2005.10.017

43. Qu W, Yuan T, Yin G, Xu S, Zhang Q, Su H (2019) Effect of properties of activated carbon on malachite green adsorption. Fuel 249:45–53. https://doi.org/10.1016/j.fuel.2019.03.058

44. Langergren S, Svenska BK (1898) Zur theorie der sogenannten adsorption geloster stoffe. Veternskapsakad Handlingar 24:1–39

45. Ho YS, McKay G (1999) Pseudo-second order model for sorption processes. Process Biochem 34: 451–465. https://doi.org/10.1016/s0032-9592(98)00112-5

46. Ahmad AA, Ahmad MA, Yahaya NKEM, Mohd Din AT, Yaakub ARW (2020) Honeycomb-like porous-activated carbon derived from gasification waste for malachite green adsorption: equilibrium, kinetic, thermodynamic and fixed-bed column analysis. Desalin Water Treat 196:329–347. https://doi.org/10.5004/dwt.2020.26067

47. Leyva-Ramos R, Ocampo-Perez R, Mendoza-Barron J (2012) External mass transfer and hindered diffusion of organic compounds in the adsorption on activated carbon cloth. Chem Eng J 183:141–151. https://doi.org/10.1016/j.cej.2011.12.046

48. Baek MH, Ijagbemi CO, O SJ, Kim DS (2010) Removal of malachite green from aqueous solution using degreased coffee bean. J Hazard Mater 176:820–828. https://doi.org/10.1016/j.jhazmat.2009.11.110

49. Gerçel Ö, Özcan A, Özcan AS, Gerçel HF (2007) Preparation of activated carbon from a renewable bio-plant of Euphorbia rigida by H_2SO_4 activation and its adsorption behavior in aqueous solutions. Appl Surf Sci 253:4843–4852. https://doi.org/10.1016/j.apsusc.2006.10.053

50. Langmuir I (1916) The constitution and fundamental properties of solids and liquids. J Am Chem Soc 38:2221–2295. https://doi.org/10.1021/ja02268a002

51. EL Hall KR, Acrivos A, Vermeulen T (1966) Pore-and solid-diffusion kinetics in fixed-bed adsorption under constant pattern conditions. Ind Eng Chem Res 5:212–223. https://doi.org/10.1021/i160018a011

52. Wang J, Guo X (2020) Adsorption isotherm models: classification, physical meaning, application and solving method. Chemosphere 258:127279. https://doi.org/10.1016/j.chemosphere.2020.127279

53. Freundlich H (1907) Über die adsorption in lösungen. Z Phys Chem 57:385–470

54. Mondal S, Majumder SK (2019) Honeycomb-like porous activated carbon for efficient copper (II) adsorption synthesized from natural source: kinetic study and equilibrium isotherm analysis. J Environ Chem Eng 7:103236. https://doi.org/10.1016/j.jece.2019.103236

55. Oepen Bv W, Kördel WK (1991) Sorption of nonpolar and polar compounds to soils:processes, measurements and experience with the applicability of the modified OECD-Guideline 106. Chemosphere 22:285–304. https://doi.org/10.1016/0045-6535(91)90318-8

56. Dotto GL, Santos JM, Rodrigues IL, Rosa R, Pavan FA, Lima EC (2015) Adsorption of methylene blue by ultrasonic surface modified chitin. J Colloid Interface Sci 446:133–140. https://doi.org/10.1016/j.jcis.2015.01.046

57. Sharma G, Sharma S, Kumar A, Naushad M, Du B, Ahamad T et al (2019) Honeycomb structured activated carbon synthesized from Pinus roxburghii cone as effective bioadsorbent for toxic malachite green dye. J Water Process Eng 32:100931. https://doi.org/10.1016/j.jwpe.2019.100931

58. Tang SH, Ahmad Zaini MA (2020) Development of activated carbon pellets using a facile low-cost binder for effective malachite green dye removal. J Cleaner Prod 253:119970. https://doi.org/10.1016/j.jclepro.2020.119970

59. Tang SH, Zaini MAA (2021) Microporous activated carbon prepared from yarn processing sludge via composite chemical activation for excellent adsorptive removal of malachite green. Surf Interfaces 22:100832. https://doi.org/10.1016/j.surfin.2020.100832

60. Azaman SH, Afandi A, Hameed B, Din AM (2018) Removal of malachite green from aqueous phase using coconut shell activated carbon: adsorption, desorption, and reusability studies. Int J Appl Sci Eng Technol 21:317–330. https://doi.org/10.6180/jase.201809_21(3).0003

61. Baytar O, Ceyhan AA, Sahin O (2021) Production of activated carbon from Elaeagnus angustifolia seeds using H_3PO_4 activator and methylene blue and malachite green adsorption. Int J Phytoremediation 23:693–703. https://doi.org/10.1080/15226514.2020.1849015